Numerical Simulation and Dynamical Response of a Moored Hydrokinetic Turbine Operating in the Wake of an Upstream Turbine

Parakram Pyakurel[1,a], James H. VanZwieten[a], Cornel Sultan[b], Manhar Dhanak[a], and Nikolaos I. Xiros[c]

[1] Corresponding Author
[a] Florida Atlantic University
[b] Virginia Tech
[c] University of New Orleans

***Abstract*—Numerical simulation of a downstream hydrokinetic turbine operating in the wake of an upstream turbine is presented. Wake effects from an upstream turbine are quantified in terms of wake velocity and amplified turbulence levels. These effects are integrated in an in-stream hydrokinetic turbine numerical simulation that utilizes a Blade Element Momentum approach with a dynamic wake inflow model. Simulations are carried out on a fixed turbine model to simulate operation in river or tidal channels with conventional foundations, as well as on a compliantly moored turbine model such as those designed to operate in open ocean currents.**

***Index Terms*— Hydrokinetic Power, Marine Renewable Energy, Ocean Current Turbines, Numerical Simulation, Wake, Turbulence.**

I. Introduction

IN-STREAM hydrokinetic turbines utilize water currents in oceans, tidal flows and rivers to produce electricity. These turbines have the potential to play a vital role in the future energy supply in many countries around the world [1], and several turbines have been designed [2, 3, 4] to harness this energy. For example, a 300 kW prototype tidal turbine was installed in the United Kingdom in 2003 [2]. Similarly, a 25 kW turbine was deployed to produce power from river currents in a remote village in Alaska [5]. A total of 14 in-stream hydrokinetic projects have been deployed so far and more than 350 other projects are planned for installation according to [6].

In-stream hydrokinetic technologies are beginning to transition from single device testing to the installation of small grid connected turbine farms. Two turbines have been deployed as the start of a small farm in Scotland [7], with eight more planned [8]. Similarly, Verdant Power has conducted prototype and pre-commercial testing of its turbines and is authorized to install up to thirty turbines in the East Channel of the East River, New York [9]. Likewise, Marine Current Turbines Ltd. plans to deploy a 10 MW array in Wales [10]. Therefore, it is important to understand the hydrodynamic interactions among turbines in an array setting to support this transition.

Experimental studies [11, 12, 13] as well as Computational Fluid Dynamics (CFD) simulations [14] have been carried out to examine wake profile behind in-stream hydrokinetic turbines. Experiments were conducted in a flume tank using three porous disks [12] and multiple turbine models [11] at different locations to simulate wake profiles of bottom mounted turbines in an array setting. The experimental setup in [13] was used to study wake profile of a single turbine in shallow water and presents analytical model based developed using a wake-similarity approach. The analytical model developed in [13] is different than the model presented here as we quantify wake velocity deficit as a function of ambient turbulence intensity (Equations 3 and 4). Moving beyond the study of the wake field alone, a CFD analysis [14] has been carried out to evaluate power produced by a downstream turbine relative to a turbine operating in the unperturbed environment.

This paper presents an approach for simulating the performance of a downstream turbine suitable for control system development and compares the open loop performance of this downstream turbine with that of a turbine operating in the unperturbed environment. The effects of upstream turbine wake are taken into account in terms of amplified turbulence and wake velocity for the evaluation of the downstream turbine performance. Algorithms utilized to quantify amplified turbulence levels and wake velocity associated with the presence of the upstream turbine [15, 16] are presented, and the integration of these algorithms into an existing numerical simulation of an Ocean Current Turbine (OCT) that uses a Blade Element Momentum (BEM) method with a dynamic wake inflow model [16, 17, 18] are discussed. Standard notations are used with boldfaced mathematical symbols representing vectors or arrays.

The downstream turbine's performance is evaluated for a bottom mounted configuration commonly used for river and tidal turbines, isolating loadings caused by the altered flow field.

Additionally, a compliantly moored turbine design, such as those under consideration for ocean current turbines, is evaluated to better understand the full system response of these devices. The bottom mounted turbine analysis only allows the rotation of turbine blades about the rotor axis (1 degree of freedom). The compliantly moored turbine analysis allows 6-degrees of freedom motions of the entire turbine system in addition to the rotation of the turbine blades about the rotor axis and the motion of the cable nodes.

Simulations of compliantly moored turbine allow analysis of the motions of the entire turbine system to support the better understanding of the expected feedback control required for the system to achieve optimal performance of a turbine array. In addition, the motion analysis of the entire turbine system enables estimation of energy required by the feedback control system to reorient downstream turbines to optimal positions.

This paper enhances numerical simulation presented in [16, 18] by integrating downstream turbulence and wake algorithms in order to evaluate performance of downstream turbine operating in a wake field of upstream turbine. First, the reference turbine used by the numerical simulation is described (Section II) in both bottom mounted and compliantly moored configurations. Then, simulation approach is discussed which includes the required coordinate transformations (Section III. A) as well as algorithms for downstream wake velocity (Section III. B) and downstream turbulence (Section III. C). The methodology for integration of algorithms presented in this paper with the turbine simulation described in [16, 19] is discussed in Section III.D. Section IV presents simulation results and discussion, followed by conclusions which are presented in Section V.

II. Reference turbine

This section presents the reference turbine model used in the numerical simulations of the upstream and downstream turbines. Fig. 1 shows a schematic diagram of the turbine deployment system (Fig. 1 top) in its moored configuration and a zoomed in view of the turbine (Fig. 1 bottom), with the same device assumed to be stationary in simulations where a bottom-mounted system is modeled. This design is nearly neutrally buoyant and has 3 blades with a rotor diameter of 20 m. The blade profile uses a FX-83-W airfoil set [19]. This airfoil was shown to produce the highest power output among 14 foil families [18] in the optimization studies that used HARP_Opt version 2.00.00 optimization routine [20]. The original design of this turbine was presented in [21] for a 3 m rotor diameter and was scaled in [18] to 20 m rotor diameter.

The details of this turbine system are provided in [18]. The mooring cable that attaches the turbine system to an anchor is 607 m long and the blades allow variable pitch. The mass of the entire modeled turbine is 500,000 kg. Relative locations of two such turbine models are varied to evaluate the wake effects of the upstream turbine on the downstream turbine.

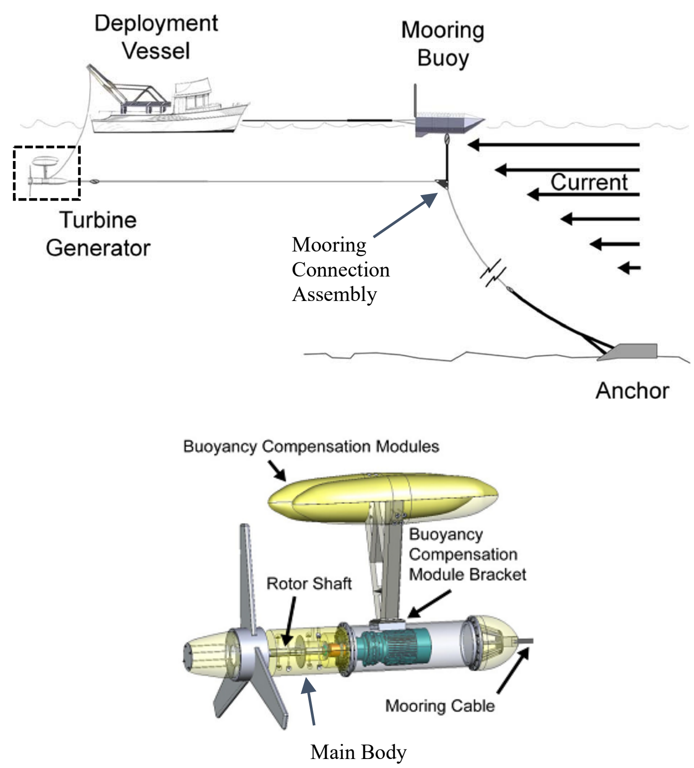

Fig. 1. Schematic diagram (not drawn to scale) of the moored system (top) with a zoomed in view of turbine (bottom).

III. Numerical simulation

Algorithms for incorporating wake velocity and amplified turbulence levels caused by an upstream turbine into the numerical simulation of a downstream turbine are presented in this section. These wake velocity and amplified turbulence level algorithms are utilized by the numerical simulation of the downstream turbine to model wake effects. Utilized coordinate systems and transformations are also discussed.

The numerical simulation utilized in this paper is not a CFD analysis. Instead, the unsteady BEM method described in [16, 18] is the simulation approach used for calculating power, torque, thrust and system response. Turbine interactions are modeled by integrating algorithms for downstream wake velocity (Equation 5) and downstream turbulence (Equation 11) to evaluate performance of downstream turbine. This unsteady BEM method calculates loadings on turbine blades by discretizing the rotor swept area and blades such that forces at each discretized element are calculated as a function of relative water velocity.

Utilized wake algorithms are for the far wake region, which is a distance exceeding 5 rotor diameters (D) downstream of the upstream turbine. The structure of the far wake region behind an upstream turbine is expressed as a function of ambient turbulence intensity and the thrust coefficient of the upstream turbine, which define the turbulence and wake velocity encountered by the downstream turbine. Hydrodynamic forces on the rotor, two buoyancy compensation modules and the main body (shown in Fig. 1) of the turbine are calculated using these modified velocity components.

A. Coordinate systems and transformations

Coordinate systems utilized for incorporating upstream turbine induced wake deficits and turbulence levels into the numerical simulation of the downstream turbine are described here, along with the associated transformation matrices. These coordinate systems include two earth fixed frames. While body fixed coordinate systems are also utilized in numerical simulations [15, 17, 18], the turbulence and wake algorithms only utilize earth fixed coordinate systems. Both earth fixed frames have a common origin that is located at the mean sea level directly above the mooring connection assembly of the downstream turbine. The mooring connection assembly is assumed to be held stationary within the water column by the larger mooring system (Fig. 1). However, for commercial systems the mooring cable will likely be attached directly to the sea floor using an anchor [22].

Two earth fixed frames used are North-East-Down (NED) frame and current fixed frame. Both these frames have common Z-axis (Fig. 2).

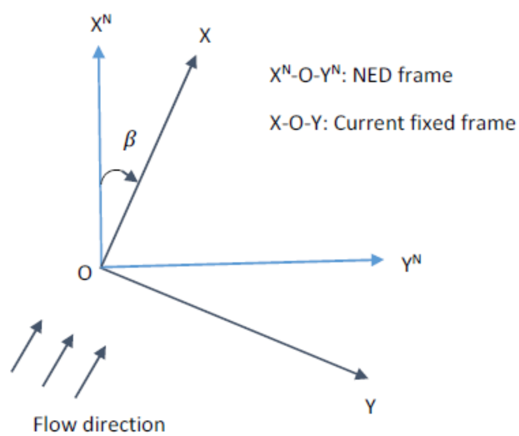

Fig. 2. Current fixed frame and NED frame.

The current fixed frame is aligned to mean flow direction with its X-axis set to the direction of the flow, Z-axis pointing downwards, and Y-axis in cross-stream direction consistent with the right hand rule. The NED frame has its X-axis pointing north, Y-axis pointing east, and Z-axis pointing downward in accordance with the right-hand-rule. This coordinate system is denoted with a superscript N in this paper and is only utilized when presenting how the wake model is integrated into the existing numerical simulation (Section III-D). Since current fixed frame is the primary earth fixed coordinate system used in this paper, no superscript is applied to variables that utilize this coordinate system. To transform variables from the current fixed frame to the NED frame, the transformation matrix, $\boldsymbol{L_{NC}}$, can be utilized. If the angle of the X-axes of the current fixed with respect to the NED frame is β, where the positive direction of β is clockwise, the transformation matrix, $\boldsymbol{L_{NC}}$, is:

$$\boldsymbol{L_{NC}}=\begin{bmatrix} c_\beta & s_\beta & 0 \\ -s_\beta & c_\beta & 0 \\ 0 & 0 & 1 \end{bmatrix}, \quad (1)$$

where c represents cosine, s represents sine, and the subscript represents the associated angle.

B. Mean wake velocity algorithm

This section presents the algorithm used to calculate the mean wake flow velocity behind a turbine, which impacts the performance of a downstream turbine. This algorithm is used to modify the inflow velocity model utilized by a downstream turbine from the one representing a turbine operating in an undisturbed flow.

The utilized analytic mean wake velocity expressions for in-stream hydrokinetic turbines were derived from wind wake models [23, 24] with coefficients optimized to represent in-stream hydrokinetic turbine wakes [15, 25]. These wake expressions calculate the reduced flow speed experienced by the downstream components as a function of flow conditions (ambient turbulence intensity), upstream turbine performance (thrust coefficient), and relative location (downstream and radial displacements). These expressions have been validated against experimental and CFD results [26].

The downstream distance between upstream and downstream turbines is calculated as the difference between the X coordinates of downstream turbine components, $\boldsymbol{X}$, and the rotor center of upstream turbine, X_u, i.e. as $\boldsymbol{X} - X_u$. Similarly, the radial distance vector, $\boldsymbol{R}$, of the downstream turbine components from the centerline of the upstream turbine is calculated as:

$$\boldsymbol{R} = \sqrt{(\boldsymbol{Y} - Y_u)^2 + (\boldsymbol{Z} - Z_u)^2}, \qquad (2)$$

where $\boldsymbol{Y}$ and $\boldsymbol{Z}$ are arrays containing all Y and Z locations of the downstream turbine components (including rotor, buoyancy compensation module and the body) on which the hydrodynamic forces are calculated, whereas, Y_u and Z_u are Y and Z coordinates of the upstream turbine rotor center.

The centerline velocity deficit vector, $\boldsymbol{U}^*$, associated with every location of the downstream turbine where hydrodynamic forces are calculated is obtained as:

$$\boldsymbol{U}^* = \frac{1-\sqrt{1-C_t}}{\left(1+2\alpha\frac{\boldsymbol{X}-X_u}{D}\right)^2}, \qquad (3)$$

where C_t is the thrust coefficient of the upstream turbine, D is the rotor diameter and α is an ambient turbulence intensity (I_o) dependent Jensen coefficient. This coefficient can be calculated as suggested in [15]:

$$\alpha = 3000\, I_o^4 - 900\, I_o^3 + 97\, I_o^2 - 3.96\, I_o + 0.0763, \qquad (4)$$

where I_o is expressed as fraction.

The final wake velocity vector experienced by the downstream turbine components can then be calculated as suggested by [15]:

$$\boldsymbol{U_w} = \boldsymbol{U_o}\left(1 - \boldsymbol{U}^*\, e^{-3.56\left(\frac{\boldsymbol{R}}{D\boldsymbol{b}}\right)^2}\right), \qquad (5)$$

where $\boldsymbol{U_o}$ is the freestream velocity vector, which is a function of vertical location, $\boldsymbol{Z}$, when a vertical shear is specified. In this equation, the parameter $\boldsymbol{b}$ is defined as:

$$\boldsymbol{b} = \sqrt{\frac{3.56\, C_t}{8\, \boldsymbol{U}^*\, (1-0.5\, \boldsymbol{U}^*)}}. \qquad (6)$$

For any turbine components where the radial distance element $\boldsymbol{R}$ is greater than or equal to its corresponding wake radius, that particular element is considered to be out of wake and experiences free a stream velocity equal to the corresponding element of $\boldsymbol{U_o}$. The wake radius is the radial distance from the rotor centerline to where the wake effect can be neglected and wake mode predictions were shown to diverge from experimental data [15]. The wake radius is calculated as suggested by [23]:

$$\boldsymbol{R^w} = \frac{1}{2} + \frac{\alpha}{D}\,(\boldsymbol{X} - X_u). \qquad (7)$$

Thus, the wake velocity on any turbine component is defined by Equation 5 only if element in $\boldsymbol{R}$ is less than the corresponding element in $\boldsymbol{R^w}$, else, the wake velocity is equal to the corresponding element of $\boldsymbol{U_o}$.

C. Downstream turbulence algorithm

This section presents an algorithm for quantifying turbulence experienced by a downstream turbine that is operating in the wake of an upstream turbine. This algorithm is presented as a function of the relative location of the downstream turbine (axial as well as radial position), ambient turbulence intensity and upstream turbine characteristics (C_t and D).

An amplified turbulence intensity vector, $\Delta\boldsymbol{I}$, is introduced that represents increased turbulence levels relative to the ambient turbulence. For a downstream turbine operating in the wake of an upstream turbine, this is calculated along the centerline according to:

$$\Delta\boldsymbol{I} = \frac{1.5}{I_o^{0.15}}\, C_t^{0.4}\left(\frac{\boldsymbol{X}-X_u}{D}\right)^k, \qquad (8)$$

where $k = -2\, I_o^{0.1}$. The centerline turbulence intensity array, $\boldsymbol{I_c}$, can then be calculated according to:

$$\boldsymbol{I_c} = \sqrt{I_o^2 + \Delta \boldsymbol{I}^2}. \tag{9}$$

The turbulence parameter array, $\boldsymbol{I_p}$, associated with the centerline location of each component of the downstream turbine is then defined as:

$$\boldsymbol{I_p} = \frac{\boldsymbol{I_c} - I_o}{I_o}. \tag{10}$$

This turbulence parameter is used to calculate the turbulence intensity array, $\boldsymbol{I_w}$, as suggested in [15]:

$$\boldsymbol{I_w} = I_o \left(\boldsymbol{I_p}\, e^{-3\left(\frac{R}{D}\right)^2} + 1\right). \tag{11}$$

The array $\boldsymbol{I_w}$ contains turbulence intensities experienced by downstream turbine components used for calculating the fluctuating turbulent velocities experienced by these components. It is also noteworthy that Equation 11 can be used at any radius, and not only up to the wake radius.

The turbulence intensity algorithms discussed above were developed to match the four sets of experimental results published in [27], [28] and [29]. Downstream turbulence intensities determined using these wake algorithms are compared with the experimentally measured values for centerline locations at ambient turbulence intensities of 3%, 7%, 9.8% and 13% (Fig. 3). A turbine model of rotor diameter 0.5 m is used by [27] with a flow velocity of 0.4 m/s. Similarly, a turbine model with a rotor diameter of 270 mm is used by [28] with a flow velocity of 0.47 cm/s. This corresponds to turbine diameter of 19 m operating in a flow velocity of 3.76 m/s based on Froude scaling [28]. In [29], a turbine model with a rotor diameter of 0.7 m is used and the flow velocity ranges from 0.4 m/s to 1.03 m/s.

In Fig. 3, the calculated turbulence intensities represented by dotted lines are obtained from Equations 8 and 9. It is seen that these equations can be used to model downstream centerline turbulence intensities with reasonable accuracy. Only one set of experimental data [29] was found during this study to be suitable for developing an algorithm for quantifying increased downstream turbulence intensity as a function of radial location. These data were collected with an ambient turbulence intensity of 3% [29]. Fig. 4 compares downstream turbulence intensity from this algorithm (Equation 11) with experimental data [29] as a function of radial location at 7 and 10 D downstream.

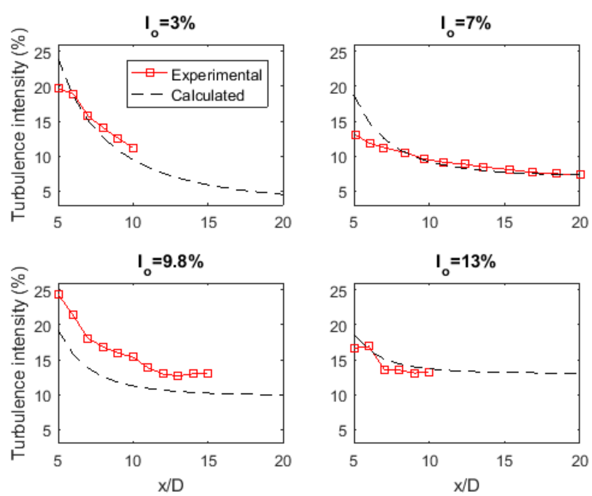

Fig. 3. Comparison of calculated and experimentally measured downstream centerline turbulence intensity.

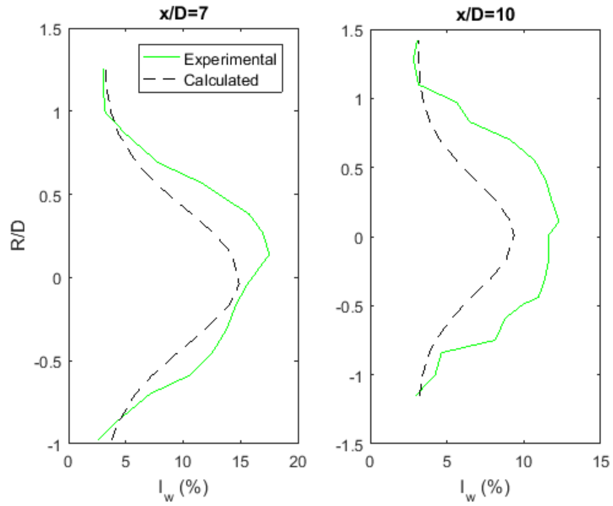

Fig. 4. Comparison of calculated and experimentally measured downstream turbulence intensity at radial locations for an ambient turbulence intensity of 3%.

From Figs. 3 and 4, it can be seen that downstream turbulence modeling algorithms (Equations 8-11) presented in this paper can predict downstream turbulence intensities for a general case without modeling specific operational characteristics such as turbine tip speed ratio and flow velocity.

D. Algorithms integration into turbine simulation

The algorithms presented above calculate the mean wake velocity (Equation 5) and turbulence intensity (Equation 11) experienced by every element of the downstream turbine. This section describes how these algorithms are integrated into the numerical simulation of the OCT presented in [16, 18]. The simulation in [18] uses unsteady BEM method and applies dynamic wake inflow model. This method divides turbine blades into a finite number of elements, with the loadings on each blade element calculated from local lift and drag coefficients obtained from local angles of attack. Loadings on every blade element are then numerically integrated to calculate tangential and axial forces in order to calculate power, torque and thrust experienced by the turbine; as well as the response of the turbine to these loadings.

The wake velocity (Equation 5) is calculated in the current fixed frame whereas the turbine simulation presented in [16, 17, 18] utilizes the velocity vector expressed in the NED frame to define the flow field. Therefore, the wake velocity obtained from Equation 5 is transformed into the NED frame using the transformation matrix $\boldsymbol{L_{NC}}$ (Equation 1) as:

$$\boldsymbol{U_w^N} = \boldsymbol{L_{NC}}\,\boldsymbol{U_w}. \quad (12)$$

A method for simulating turbulent flow on a moored in-stream hydrokinetic turbine was presented in [16]. This method computes turbulent flow velocities as a function of time and location, with turbulence intensity and time averaged mean flow velocity as main input parameters. In this method, a velocity spectrum is integrated over a considered frequency range to obtain equations that express this spectrum as a function of turbulence intensity. Desired spatial correlation is obtained by multiplying the spectrum with a coherence function. Cholesky's decomposition is then carried out on the spectrum to obtain fluctuating velocity components in the frequency domain. These fluctuating velocity components are converted into time domain by considering turbulence as a combination of sine waves that contain all discretized frequencies within the considered frequency range.

The fluctuating turbulence velocity component matrix for a turbine in an unperturbed flow, $\boldsymbol{u_u}$, associated with I_o is obtained by calculating u, v and w components of $\boldsymbol{u_u}$ in streamwise, cross-stream and vertical directions respectively. For a discretized element j, if u_j, v_j and w_j are the u, v and w components of $\boldsymbol{u_u}$, the correlated value of u_j denoted by u_j^e is calculated as:

$$u_j^e(t) = u_j(t) + r_{uv}v_j(t) + 2r_{uw}w_j(t), \quad (13)$$

where r_{uv} is the correlation coefficient between u and v and r_{uw} is the correlation coefficient between u and w. A combination of a sine wave function with summation of all frequencies as shown below is utilized [16] to calculate u_j, v_j and w_j:

$$m_j(t) = \sum_{k=1}^{N} |m_{kj}^*| \sin\left(2\pi f_k^* t + \theta_{kj}^R\right), \quad (14)$$

where m_j= u_j, v_j and w_j; m_{kj}^* is obtained from Cholesky's decomposition of the spectra [16]; N is the total number of frequency components; f_k^* is k^{th} frequency component, t is time and θ_{kj}^R is the resultant phase associated with j and k.

The velocity spectra utilized for Cholesky's decomposition in this paper is assumed to follow Kolmogorov's five thirds law, where the velocity power spectral density is proportional to the negative five third power of frequency. Hence, the slope of the spectra is the same for all turbulence intensities in logarithmic scale. However, the magnitude of variance and in turn, standard deviations vary with turbulence intensity. Therefore, if the magnitudes of the simulated fluctuating velocity components of the upstream turbine presented above are adjusted, they can be utilized to simulate velocity components experienced by the downstream turbine.

Velocity standard deviations dictate the magnitude (amplitude) of fluctuating velocity components. Since linear relationship exists between velocity standard deviations and turbulence intensity for a given mean flow velocity, the amplification factor presented in the equation below can be applied to obtain fluctuating velocity components (Equation 14) for the downstream turbine associated with $\boldsymbol{I_w}$:

$$\boldsymbol{u_t} = \frac{\boldsymbol{I_w}\,\boldsymbol{U_w}}{I_o\,\boldsymbol{U_o}}\,\boldsymbol{u_u}, \qquad (15)$$

where $\boldsymbol{u_t}$ is the fluctuating velocity matrix of downstream turbine that includes wake effects and is a function of time. It is noteworthy that $\boldsymbol{u_u}$ and $\boldsymbol{u_t}$ contain all three components of the fluctuating velocity in X, Y and Z directions in the current fixed frame.

It may be pointed out that $\boldsymbol{u_t}$ can alternatively be obtained by applying the same simulation method [16] utilized for determining $\boldsymbol{u_u}$ by changing the input parameters from I_o and $\boldsymbol{U_o}$ to $\boldsymbol{I_w}$ and $\boldsymbol{U_w}$. However, we have utilized Equation 15 for calculating $\boldsymbol{u_t}$ to reduce computation time. To integrate this these turbulent fluctuations into the existing numerical simulation [18] they are converted into the NED frame by:

$$\boldsymbol{u_t^N} = \boldsymbol{L_{NC}}\,\boldsymbol{u_t}. \qquad (16)$$

The final resultant velocity, $\boldsymbol{U^N}$, experienced by the downstream turbine after including wake, turbulence and wave velocities in the NED coordinate system is obtained as:

$$\boldsymbol{U^N} = \boldsymbol{U_w^N} + \boldsymbol{u_t^N} + \boldsymbol{u_v^N}, \qquad (17)$$

where $\boldsymbol{u_v^N}$ is the wave induced velocity vector described in [18], $\boldsymbol{U_w^N}$ is the wake velocity vector (Equation 12), and $\boldsymbol{u_t^N}$ is the fluctuating turbulence velocity array (Equation 16).

Spatial grids containing elements of buoyancy compensation modules, the main body and rotor elements are not likely to be precisely perpendicular to the mean flow direction, especially for a moored turbine. However, the turbulence simulation [16] is developed based on the assumption that all locations where turbulent fluctuations are calculated are set to a fixed grid that is perpendicular to the direction of the mean flow. This may lead to small errors in the phase of the turbulent structures on turbine components that are either upstream or downstream from the center of the mesh grid.

IV. Results and discussions

This section presents simulation results for a downstream turbine and compares them with the performance of a turbine operating in an unperturbed flow. This is done to quantify the relationship between relative turbine location and performance. The numerical simulations were run using a standard 8 core computers and run times were sensitive to the motions induced on the turbine because of the cable model. For this reason, it took on average about 4 hours to run a 30 minute simulations when the downstream turbine was assumed to be stationary (i.e. no cable model) and about 9 hours to run 30 minute simulations when the response of the downstream compliantly moored turbine was considered.

To compare simulation results with experimental findings, simulations are first carried out to match the ambient turbulence intensities of experimental results in [11] (sub-section A). Then, additional simulations are carried out for a bottom mounted turbine where only rotor rotation is allowed (sub-section B) and for a compliantly moored turbine system where translation and rotation motions about all axes are allowed (sub-section C). The mean flow velocity of 1.6 m/s is utilized for both bottom mounted and compliantly moored turbine cases. In the bottom mounted turbine analysis, the rpm of the rotor is maintained at the constant speed associated with the optimal tip speed ratio of the turbine assuming that the flow only varies spatially and not temporally. Since the downstream turbine experiences different mean velocities at different blade elements caused by wake shear, the spatial average of velocity over the swept area of the rotor is utilized to determine optimal rpm. In the moored turbine analysis, a standard wind turbine torque control approach that utilizes the constant gain torque controller presented in [30] is applied to control the rpm of the rotor.

A. Comparison with a previous study

Our simulation results are compared with experimental results presented in [11]. Simulations are run using algorithms presented here for a bottom mounted turbine at axial distances of 6, 8, 10 and 12 D behind the upstream turbine rotor center for an I_o of 3%. Simulations were also performed for axial distances of 5, 6, 8 and 10 D for an I_o of 15%. The ambient turbulence intensities and downstream axial distances stated above were selected to match the experimental conditions in [11]. These simulations were each run for a simulated time of 5 minutes. The experiments in [11] were conducted on bottom mounted 3-bladed prototypes of horizontal axis turbines with diameters of 0.7 m.

To visualize the wake propagation associated with these conditions, model predicted mean wake velocity and turbulence intensity fields behind a single turbine are presented for these two turbulence intensities. Fig. 5 a-b shows the mean velocity for ambient turbulence intensities of 3 and 15%, while Fig. 5 c-d shows the turbulence intensity fields for these two ambient turbulence intensities respectively. These figures are created assuming that the thrust coefficient is 0.83. It is noted that it is not necessary to simulate the flow field over the area presented here to simulate downstream turbine performance. Since these equations model the far-wake field which typically starts around five diameters downstream only distances beyond this are shown. For both turbulence intensities, the wake deficit persists much further downstream than the increased turbulence intensity values in the wake field. These results also show that the velocity in the far-wake is lower and persists longer for lower turbulence intensities. They also suggest that turbulence intensity values nearly reach their ambient values at 13 diameters downstream for both of the evaluated ambient turbulence intensities.

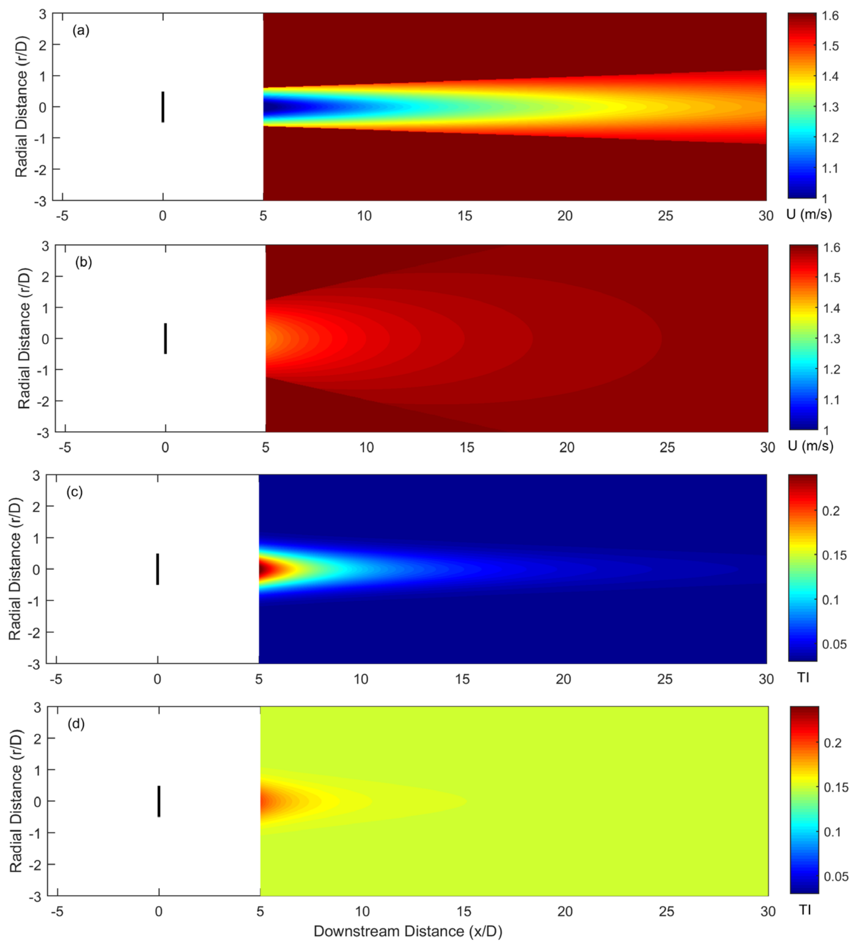

Fig. 5. Mean wake velocities calculated for ambient turbulence intensities of 3% (a) and 15% (b), and turbulence intensity calculated for ambient turbulence intensities of 3% (c) and 15% (d) in the far wake region behind in-stream hydrokinetic turbines.

It is noted that environmental/ambient conditions other than the turbulence level and thrust coefficients such as bathymetry, blockage ratio and tip speed ratio also affect wake decay and in turn, downstream power. Therefore, the numerical simulations are not expected to exactly model the experimental conditions of [11] since these conditions were not considered when developing this numerical simulation. Instead, the developed numerical simulation approach aims to provide estimates of downstream turbine performance using computationally inexpensive and relatively fast algorithms that do not model the detailed operating conditions. These algorithms are generic in that they were optimized based on multiple experimental data sets from a range of potential tidal turbine operating conditions. In other words, the simulations are not carried out to exactly model the experimental setup in [11], or any other experimental setup, but to calculate the approximate downstream turbine power and loadings. Therefore, while quantitative differences between the results reported in [11] and our simulation results are expected, the qualitative trends should be similar. Furthermore, algorithms presented in this paper are optimized based on turbine models that were scaled either using Froude number or thrust coefficient [15] and therefore, we believe that our analyses with much larger turbine as discussed in following sections are valid even though the validation here is carried out with small turbine model.

Note also that one of the key applications of the models and numerical simulations presented herein will be in feedback control design for turbines. For this purpose, striving to achieve perfect reproduction of an experimental condition is not deemed necessary. For feedback control design the presented numerical simulation will be augmented with perturbation models to account for modeling errors, uncertainties, and sensor measurement errors. Numerous modern control techniques have been developed to mitigate the perturbations and have reached a stage of maturity to enable their implementation in realistic systems. For example, we have successfully used such techniques in [31] for the flight control of a moored ocean current turbine.

Mean power produced by the downstream turbine at axial distances from the upstream turbine rotor center (co-axial case) of 6 D, 8 D, 10 D and 12 D for I_o=3% are calculated to be 41%, 46%, 49% and 53% of upstream turbine power respectively in the simulations, whereas these corresponding values in [11] are 23%, 35%, 47% and 53%. Similarly, for I_o=15%, the power produced by the downstream turbine at 5 D, 6 D, 8 D and 10 D are calculated to be 77%, 80%, 85% and 90% of the upstream turbine power in the simulation whereas these corresponding values are about 80%, 88%, 90% and 92% of in [11]. These results are presented pictorially in Fig. 6. In this figure the downstream distance is normalized using rotor diameter, x/D, where, x is the axial distance between upstream and downstream turbine rotor centers. It is seen that experimental and simulation results show the same qualitative trends and have relatively good agreement beyond 9 D. Since downstream turbines are likely to be placed beyond 9 D, we can conclude that the simulation algorithms presented in this paper can be utilized to assess downstream turbine performance.

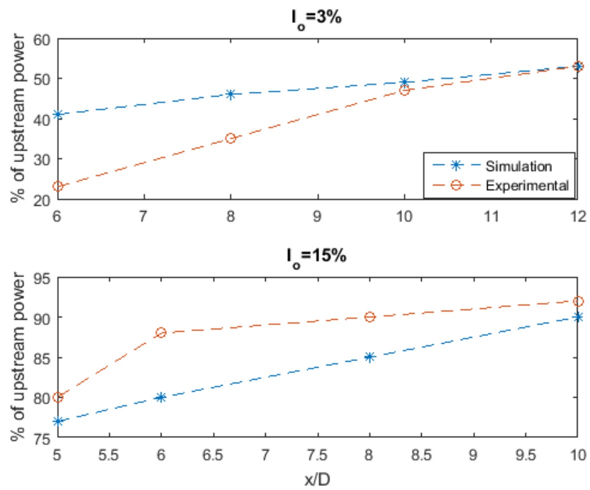

Fig. 6. Comparison of experimental and simulation results for downstream turbine power.

In order to point out the effects of the operating conditions on the downstream turbine power, it is worth mentioning a Computational Fluid Dynamics (CFD) based analysis presented in [14]. The study in [14] had a blockage ratio of about 1.3% which is different from study in [11] where the blockage ratio was about 4.8%. The CFD predicted power output of the downstream turbine at 10 D and 40 D were 29.3% and 82.8% of the upstream turbine respectively in [14] for I_o= 0.68%. These results are very different from the experimental results in [11] and show the effects of boundary/experimental conditions in addition to ambient turbulence intensity on the downstream turbine power.

B. Simulation results for the bottom mounted system

Simulations are carried out for ambient turbulence intensity (I_o) values of 5% and 10% for the bottom mounted turbine. The I_o value of 10% is considered as two tidal sites have shown this value for a wide range of mean flow speed [32]. Similarly, an I_o value of 5% is considered because OCTs will operate in deep water away from most boundary effects as opposed to tidal turbines that operate in shallow water and much closer to boundaries. Therefore, it is assumed that ambient turbulence at open ocean energy sites will be less than at tidal sites. For the results in this section, simulations are performed to generate 30 minute time histories for each evaluated operating condition. Results are first presented for a case where downstream turbine location is co-axial with upstream turbine, and then for downstream distance of 10 D as a function of radial location.

Fig. 7 shows time histories of shaft power for I_o= 5% and 10% calculated using the bottom mounted turbine simulation. Power produced by the downstream turbine is calculated at normalized axial distances (x/D) of 5, 10 and 15. For I_o= 5% (Fig. 7 left), the mean powers produced by the downstream turbine at axial distances of 5 D, 10 D and 15 D are 41.6%, 52.6% and 61.7% of the mean power produced by the upstream turbine. The standard deviations of power for the upstream turbine is 5.8% of the mean upstream power, whereas the power standard deviations are 19.6%, 9.7% and 6.9% of the corresponding mean power values for the respective axial distances.

For I_o= 10% (Fig. 7 right), the mean power produced by the downstream turbine at axial distances of 5 D, 10 D and 15 D are 51.8%, 67.2% and 76.8% of the power produced by the upstream turbine. The power standard deviation for the upstream turbine is 11.7% of mean power, whereas these deviations are 18.2%, 13.5% and 13.1% of the mean power produced at their respective downstream distances. By comparing the results for the two turbulence intensities it can be seen that downstream power recovery happens more quickly as ambient turbulence intensity increases because of the associated faster wake recovery.

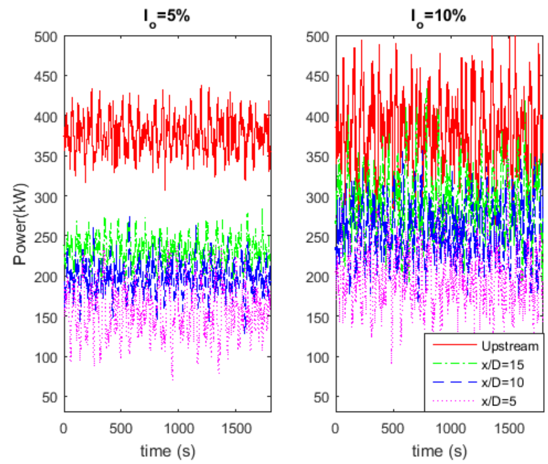

Fig. 7. Power time history at axial locations for I_o= 5% (left) and 10% (right) for bottom mounted turbine.

Fig. 8 shows mean and standard deviation power trends over a wider range of downstream distances (5-30 D). The presented standard deviations are normalized by dividing these deviations by their corresponding mean power at a given location. It is seen that for I_o= 5%, the mean power converges from 41.6% to 78.5% of free stream as downstream distance is changed from 5 D to 30 D. Another observation is that the power standard deviation converges back to the upstream value more quickly than mean power, converging from 19.6% to 9.7% for downstream distances of 5 D and 10 D and then to 6.4% at 30 D. This 30 D standard deviation is only 0.6% higher than the free stream value.

For I_o= 10%, mean power converges from 51.8% to 90.0% of free stream as downstream distance is changed from 5 D to 30 D. These results also show that the standard deviation converges rapidly as a function of downstream distance, converging from 18.2% to 13.5% for downstream distances of 5 D and 10 D and then to 13.3% at 30 D (1.6% higher than free stream). It is noted that downstream power converges more rapidly back to the upstream value for the higher ambient turbulence intensity. Also, it is seen that wake effects on mean power persist beyond 30 D for both values of I_o, but that the variation in power has nearly converged to upstream values by this distance.

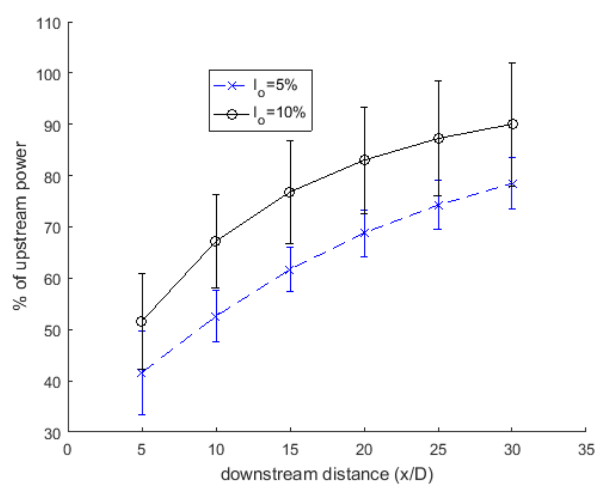

Fig. 8. Power at different downstream distances with standard deviations for I_o= 5% and 10% for bottom mounted turbine.

Since turbulence and shear cause fatigue on turbine blades due to the time varying loads that they produce, axial forces on a single turbine blade are examined for I_o= 5% and 10%. Axial forces on one blade of the tri-bladed rotor are evaluated at locations ranging 5 D to 30 D downstream. The time averaged mean and standard deviations of the axial load on this blade are presented in Fig. 9, along with the time averaged and standard deviations for a turbine operating in the free stream (dashed line). Since the mean forces for I_o= 5% and 10% are nearly equal (force for I_o= 10% is only 0.31 kN greater than I_o= 5%), both mean forces are represented by a single dashed horizontal line. The vertical bars on this line are standard deviations for I_o= 5% (shorter bar) and I_o= 10% (longer bar). It is seen that mean axial forces at 30 D are still lower than upstream value for both values of I_o (15.2% lower for I_o= 5% and 6.8% lower for I_o= 10%), indicating that wake velocities that cause axial force have not recovered to upstream value. At 10 D downstream and beyond, the axial force standard deviations are within ±11% of upstream standard deviation. These force variations are increased by the amplified turbulence intensities in the wake but decreased by the mean flow speed being reduced. These effects roughly offset each other for co-axial turbines separated by more than 10 D downstream.

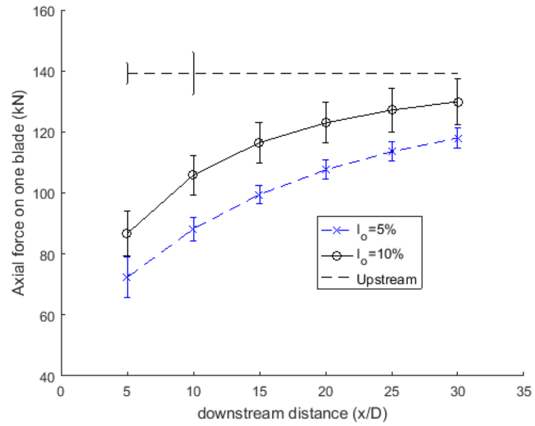

Fig. 9. Axial force downstream for I_o= 5% and 10% for bottom mounted turbine.

Turbines will seldom operate precisely co-axially with each other and therefore a comparison is made between power produced by upstream turbine and a downstream turbine as a function of radial location. This comparison is conducted for an axial downstream distance of 10 D. Time histories of the power produced for R/D = 0.5 are shown in Fig. 10, along with power produced by downstream turbine at R/D=0 and an upstream turbine. For I_o= 5%, the power produced by downstream turbine at R/D=0.5 is found to be about 70% of upstream turbine power and 33% higher than power produced at R/D=0 (Fig. 10 left). For I_o= 10%, the power produced by downstream turbine at R/D=0.5 is found to be about 74.6% of upstream turbine power and 11% higher than power produced at R/D=0 (Fig. 10 right).

It is noteworthy that power produced by a turbine at R/D=0.5 and axial distance of 10 D is higher for I_o= 5% than for I_o= 10%. This is because the wake radius increases with increasing ambient turbulence intensity as experimentally observed [27], causing wake velocity at R/D=0.5 for I_o= 5% to be higher than for I_o= 10%. However, the power produced by turbine for I_o= 10% at R/D=0 and a downstream distance of 10 D is about 28% higher than the power produced by turbine for I_o= 5% at the same location. This is because the wake decays faster in the direction of flow for higher turbulence intensity although it propagates with greater radius as the turbulence intensity increases. Power standard deviation at R/D=0.5 is 17% higher than the value at R/D=0 for both I_o= 5% and 10%.

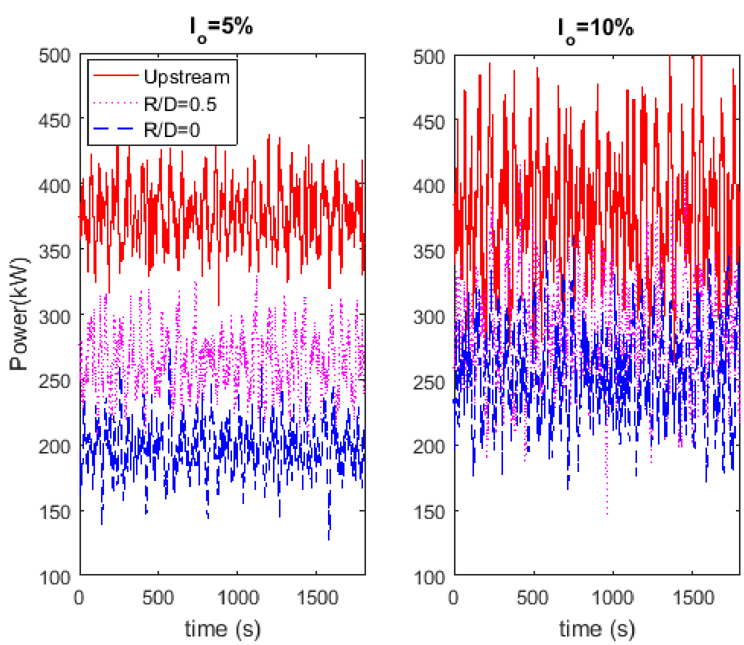

Fig. 10. Power time history at radial locations for I_o= 5% (left) and 10% (right) for bottom mounted turbine case at centerline distance 10 D.

In order to better visualize the relationship between power production and radial location, the percentage of upstream power produced for a range of radial locations is presented for a downstream distance of 10 D (Fig. 11). The percentage values are the time averaged means for ambient turbulence intensities of I_o= 5% and 10%. The fluctuation of power due to turbulence are shown as standard deviation bars. These deviations are normalized using their corresponding individual power production values. It is noted that the power produced increases as radial distance increases with power produced almost equal to upstream power starting R/D= 1.25 for both I_o= 5% (100% recovery) and I_o= 10% (around 98% recovery). The normalized standard deviations of power are lowest at R/D=0 for both I_o values and increase with increased radial distance up to R/D=1.25 where the turbine is nearly out of wake, and these deviations approach upstream values.

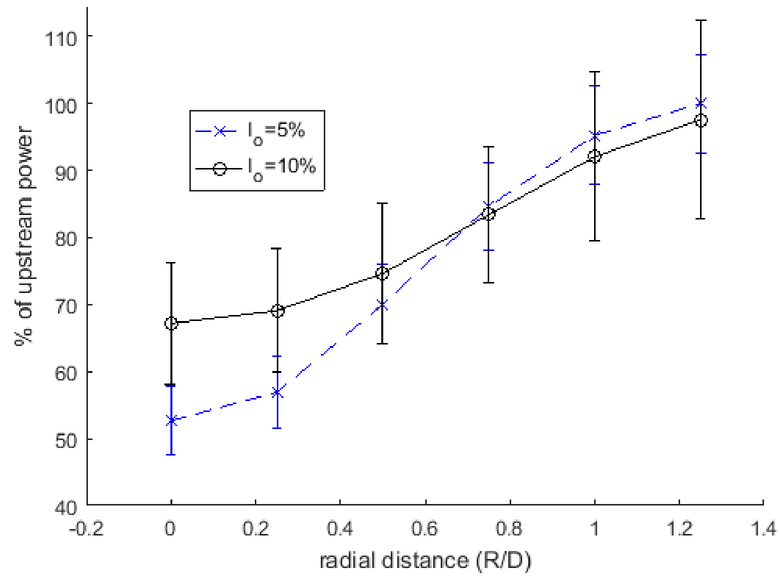

Fig. 11. Downstream power variation with radial distance for axial distance of 10 D.

Time averaged values of the axial force experienced by one blade of the tri-bladed rotors are presented as a function of radial locations for a centerline distance of 10 D in Fig. 12. The dotted horizontal line is upstream value and vertical bars in this line represent standard deviations for I_o= 5% (short bar) and I_o= 10% (long bar). It can be seen that axial forces converge back to upstream value at R/D= 1.25. The standard deviation of axial force fluctuation is presented using error bars. At R/D= 1.25, it can be noted that the standard deviation for I_o= 10% is higher than for I_o= 5% although the mean values are almost same. The standard deviation is highest at R/D=0.75 for I_o= 5%, whereas it is highest at R/D=1 for I_o= 10%. This difference is likely caused by different wake radii, downstream turbulence values and wake velocities associated with different I_o values.

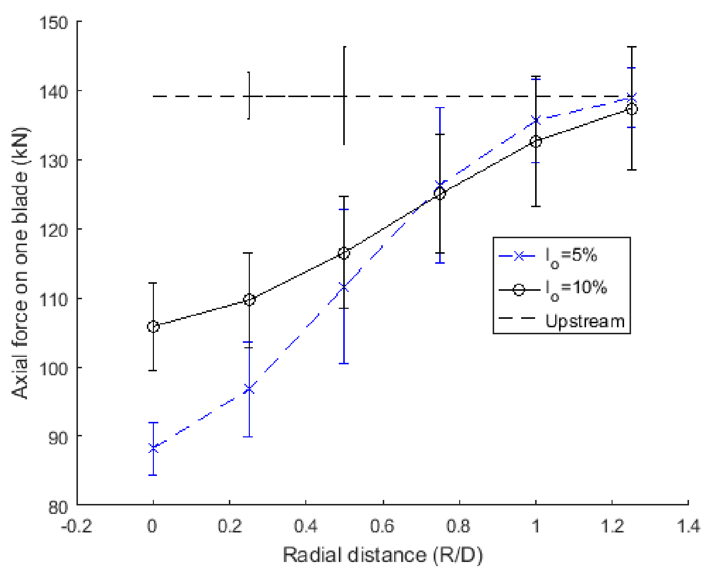

Fig. 12. Axial force variation with radial distances at axial distance of 10 D.

C. Simulations results for moored system

The performance of a compliantly moored downstream turbine is simulated to evaluate the power, motion and axial loading. Motion analysis is an important part of this process as this turbine system is free to move, changing its location and therefore the temporally and spatially varying wake effects. In most cases, simulations are run to simulate a period of 30 minutes and ambient turbulence intensities of I_o= 5% and 10% are utilized. In the first analysis, the downstream turbine is anchored such that it would operate co-axially with the upstream turbine at downstream distances of 5 D, 10 D and 15 D if the flow were steady and undisturbed by the upstream system. After this, numerical simulations are run where the downstream turbine would operate at a downstream distance of 10 D and radial distances of 0.5 D if deployed in a steady and unperturbed flow.

Power time histories are shown for the three nearly co-axial simulations in Fig. 13. For I_o= 5% (Fig. 13 left), time averaged axial distances for a period of 30 minutes are found to be 4.5 D, 9.7 D and 14.8 D with corresponding time averaged mean radial distances of 0.15 D, 0.05 D and 0.02 D. This shows that the wake from the upstream turbine reduces the loading on the downstream turbine causing it to operate slightly upstream from where it would operate if the flow were undisturbed. Minimal lateral motions are also induced on the turbine caused by the turbulence and wake shear. Mean power produced by downstream turbine at these locations are 44.4%, 52.8% and 61.9% of power produced by upstream turbine respectively. These powers are similar to bottom mounted turbines, except for a downstream distance of 5 D where the moored turbine producing slightly more power (about 3%) than the bottom mounted turbine likely due to a slight radial misalignment. The power standard deviation is 2.6% of mean power for an upstream moored turbine, whereas these deviations for the three downstream distances are 9.7%, 4.7% and 4.3% of their respective mean values.

For I_o= 10% (Fig. 13 right), time averaged axial distances for a period of 30 minutes are found to be 4.7 D, 9.8 D and 14.9 D with corresponding radial distances of 0.08 D, 0.03 D and 0.04 D. The faster wake decay associated with this I_o is responsible for the turbine being located slightly further downstream than for I_o= 5%. Mean power produced by downstream turbine at these locations are about 51.9%, 67.3% and 76.9% of power produced by upstream turbine respectively. The power standard deviation is 4.5% of mean power for upstream turbine, whereas these deviations are 9.7%, 8.1% and 7.6% of mean power for the three downstream distances. It is seen that for both I_o values, the percentage of power standard deviation with respect to the corresponding mean values is 9.7% for downstream distance of about 5 D (for 4.5 D at I_o= 5% and for 4.7 D at I_o= 10%). This almost same percentage value (9.76 % for I_o= 5% and 9.78 % for I_o= 10%) is likely only a coincidence.

Although not directly comparable with the bottom mounted turbine because of the moored turbine motion and different rotor control strategies, the overall downstream power for co-axial cases are very similar for the moored and bottom mounted turbines. However, the standard deviations percentages are higher for bottom mounted turbine than for moored turbine. This is most likely caused by the difference in the utilized rotor speed control strategies, as well as the compliance of the mooring cable reducing relative velocities by allowing the turbine to move slightly downstream during peak flow speeds.

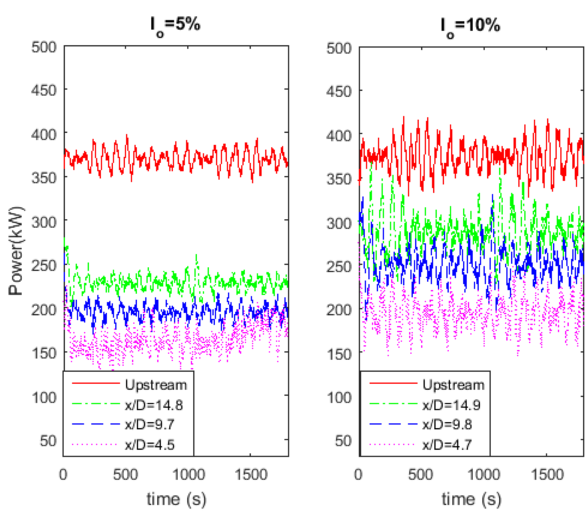

Fig. 13. Power time history at approximate axial locations for I_o= 5% (left) and 10% (right) for moored turbine.

Simulations are carried out to evaluate the performance of a moored downstream turbine when its initial position is set at radial location of 0.5 D and axial distance of 10 D relative to upstream turbine rotor center. These results are compared with those obtained for R/D =0. Ambient turbulence intensities of I_o= 5% (Fig. 14) and I_o= 10% (Fig. 15) are evaluated. It can be seen that when a downstream turbine is initially placed at radial location of 0.5 D, it is found to move towards the centerline where velocity is low for both turbulence intensities.

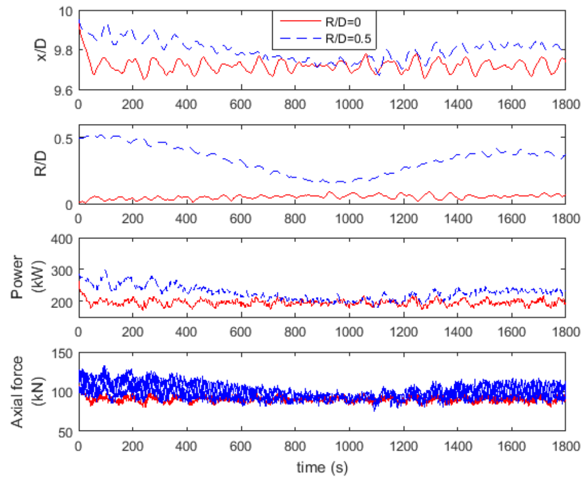

Fig. 14. Comparison of moored downstream turbines for two initial radial positions for I_o= 5%.

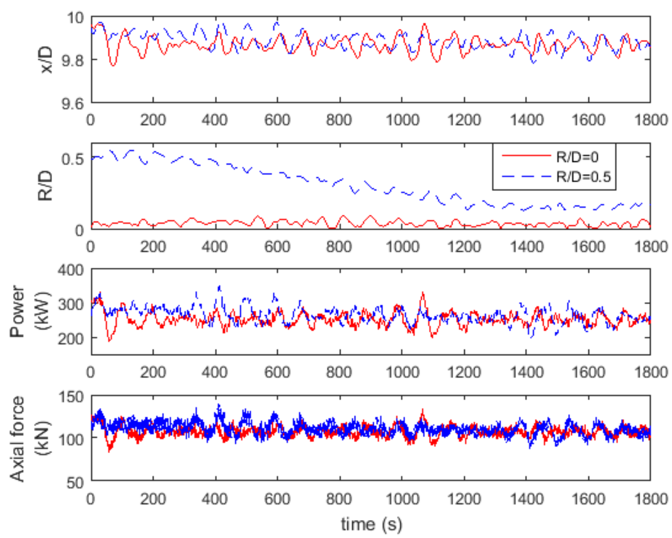

Fig. 15. Comparison of moored downstream turbines for two initial radial positions for I_o= 10%.

It can be seen in Figs. 14 and 15 that when the unperturbed turbine position is co-axial, i.e. R/D =0, the turbine position is less variable than for R/D =0.5. This is because both the mean wake and the cable forces are pulling the turbine towards the same equilibrium location for R/D =0. Conversely, for the R/D =0.5 case, the time averaged cable forces and the wake forces pull the turbine in opposite directions. Therefore, the turbine tends to oscillate with a mean location between these locations with oscillations excited by the time varying turbulence field.

Lower ambient turbulence intensities leads to more consistent and pronounced shear regions within wake, because there is less mixing between different velocity layers at low turbulence levels. Therefore, velocity regions inside wake are more pronounced and consistent for I_o= 5% than for I_o= 10% (bottom figures in Fig. 14 & Fig. 15). Additionally, wake velocity recovery at a given co-axial/centerline distance is greater for higher turbulence intensity causing less wake velocity shear for I_o= 10% than for I_o= 5%.

In order to better visualize the long term motion behavior of turbine system, simulation is run to generate turbine position time histories of 3 hours for I_o= 5% and I_o= 10% with the downstream turbine center position set to radial and axial distances of 0.5 D (10 m) and 10 D (200 m) respectively. Y (cross-stream) and Z (vertically downwards) positions of downstream turbine relative to upstream turbine are plotted for I_o= 5% (Fig. 16 left) and 10% (Fig. 16 right), with the figures plotted as if the turbine was observed from a downstream location. The positions are normalized by rotor diameter and hence there are no units.

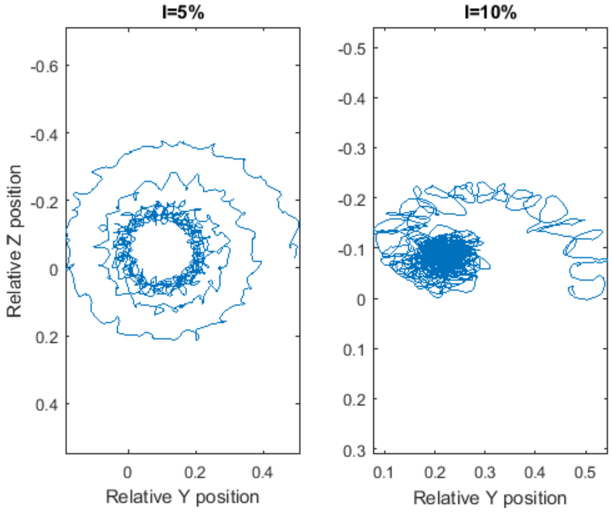

Fig. 16. Relative Y and Z positions (normalized by rotor diameter) of downstream moored turbine with respect to upstream turbine.

It can be seen in Fig. 16 that the travel range for I_o= 5% is higher than for I_o= 10%, which is caused by higher wake velocity shear values. Position fluctuations are caused by combined effects of cable force on turbine system, shear force and turbulence. For I_o= 5%, the shear values are relatively high and resulting forces are more dominant than for I_o= 10%, resulting in a more easily observable periodic motion stemming from the interplay of shear and cable forces. The amplitudes of both Y and Z motions eventually stabilize at the value of around 0.125 D for both Y and Z axes (Fig. 16 left). For I_o= 10%, turbulence induced motions are more pronounced and the lateral forces (shear and cable forces) approximately balance one another (Fig. 16 right). In this case, the amplitudes of both Y and Z motions eventually stabilize at the value of around 0.0375 D

Overall, it is noted that shear causes the downstream turbine to move towards the centerline of upstream turbine where both relative Y and Z positions are 0. On the other hand, turbulence causes random motion and the cable force tend to move the turbine away from centerline because it is anchored at radial position of 0.5 D.

V. Conclusions

The wake caused by an upstream turbine is quantified in terms of mean wake velocity and amplified turbulence. These downstream effects are integrated into the numerical simulation of a downstream turbine. The performance of the downstream turbine at different locations relative to the upstream turbine is then evaluated. Simulations are performed for bottom mounted and compliantly moored turbine systems.

Higher turbulence levels are found to increase the power produced by a co-axially located downstream turbine because the wake effects converges towards unperturbed values more quickly. The impact downstream and radial location have on power production are quantified for bottom mounted and moored turbine systems. Motion analysis of a downstream moored turbine is performed and it is observed that this turbine moves towards the centerline region of the upstream turbine when its radial position is set to be away from the centerline of the upstream turbine.

The mathematical models and simulation results obtained here can be used for array layout optimization. In addition, the models and results for compliantly moored turbine can be used in the design and analysis process of feedback control systems required to control the position and the orientation of downstream turbines in a turbine array. In light of the results reported herein, feedback flight control is found to be important for the stabilization of the downstream turbines operating in the wake of upstream turbines in an array. Our results show that downstream turbines tend to move to the centerline region of the upstream turbine, which will reduce power production and for multiple turbine arrays could lead to collisions. This problem can be solved using collision avoidance trajectory path planning and control. Also, in order to reconfigure and distribute an array of turbines for optimal ocean current energy harvesting, formation flight control based on the models and simulations presented herein is mandatory.

VI. ACKNOWLEDGEMENT

We would like to thank National Science Foundation (NSF) and specifically the Energy, Power, Control and Networks (EPCN) program within the framework of grant ECCS-1307889 'Collaborative Research: Optimized Harvesting of Hydrokinetic Power by Ocean Current Turbine Farms Using Integrated Control' for funding this project.

VII. References

[1] F. O. Rourke, F. Boyle, and A. Reynolds, A., "Marine current energy devices: Current status and possible future applications in Ireland," *Renewable and Sustainable Energy Reviews*, vol. 14, Issue 3, pp. 1026-1036, 2010.

[2] P. L. Fraenkel, "Marine current turbines: pioneering the development of marine kinetic energy converters," in *Proc. IMechE vol. 221 Part A: J. Power and Energy,* 2006.
[3] K. Kubo, Y. Kabata, K. Nakamura, S. Nagaya, and T. Ueno, "Development of blade for floating type current turbine system," *Oceans - St. John's*, 2014.
[4] J. N. Goundar, and M. R. Ahmed, "Marine current energy resource assessment and design of a marine current turbine for Fiji," *Renewable Energy*, vol. 65, pp. 14-22, 2012.
[5] ORPC press release, "ORPC's RivGen Power System Delivers Power to Remote Alaskan Village Grid," *Ocean Renewable Power Company*, Jul., 2015, [Online]. Available: http://www.orpc.co/newsevents_pressrelease.aspx?id=iNre8ZETbAA%3d, (Accessed: May 24, 2016).
[6] Marine and Hydrokinetic Technology Database, [Online]. Available: http://en.openei.org/wiki/Marine_and_Hydrokinetic_Technology_Database, (Accessed: July 5, 2016).
[7] Renewable Energy World. [Online]. Available: http://www.renewableenergyworld.com/articles/2016/09/scotland-welcomes-world-s-first-grid-connected-commercial-tidal-power-array.html (Accessed: September 22, 2016).
[8] Tidal Energy Today. [Online]. Available: http://tidalenergytoday.com/2016/02/24/tocardo-to-test-t2-tidal-array-at-emec/ (Accessed: September 22, 2016).
[9] Verdant Power. [Online]. Available: http://www.verdantpower.com/rite-project.html (Accessed: July 5, 2016).
[10] Marine Current Turbines: An Atlantis Company, [Online]. http://www.marineturbines.com/3/news/article/44/marine_current_turbines_kicks_off_first_tidal_array_for_wales (Accessed: September 22, 2016).
[11] P. Mycek, B. Gaurier, G. Germain, G. Pinon, and E. Rivoalen, "Experimental study of the turbulence intensity effects on marine current turbines behaviour, Part II: Two interacting turbines," *Renewable Energy*, 68 (2014) 876-892, 2014.
[12] L. E. Myers, and A. S. Bahaj, "An experimental investigation simulating flow effects in first generation marine current energy converter arrays," *Renewable Energy*, 37 (2012) 28-36, 2012.
[13] T. Stallard, T. Feng, and P.K. Stansby, "Experimental study of the mean wake of a tidal stream rotor in a shallow turbulent flow," *Journal of Fluids and Structures*, Volume 54, pp. 235–246, April 2015.
[14] R. Malki, I. Masters, A. J. Williams and T. N. Croft, "Planning tidal stream turbine array layouts using a coupled blade element momentum - computational fluid dynamics model," *Renewable Energy*, 63 (2014) 46-54, 2014.
[15] P. Pyakurel, J. H. VanZwieten, and M. Dhanak, "Numerical Simulation of an Ocean Current Turbine Operating in a Wake Field," *PhD Dissertation, Florida Atlantic University,* 2016. [Online]. Available: http://purl.flvc.org/fau/fd/FA00004737 (Accessed: Apr. 27, 2017).
[16] P. Pyakurel, J. H. VanZwieten, M. Dhanak, and N. I. Xiros., "Numerical modeling of turbulence and its effect on ocean current turbines," *International Journal of Marine Energy*, vol. 17, pp. 84-97, 2017.
[17] J. H. VanZwieten, N. Vanrietvelde, and B. L. Hacker, 2013, "Numerical Simulation of an Experimental Ocean Current Turbine," *IEEE Journal of Oceanic Engineering*, vol. 38, No. 1, 2013.
[18] J. H. VanZwieten, P. Pyakurel, T. Ngo, C. Sultan, and N. I. Xiros, "An assessment of using variable blade pitch for moored ocean current turbine flight control," *International Journal of Marine Energy*, vol. 13, pp. 16-26, 2016.
[19] UIUC Applied Aerodynamics Group, 'Airfoil Coordinates Database. Department of Aerospace Engineering, University of Illinois at Urbana-Champaign, 2011, [Online]. Available: http://www.ae.illinois.edu/m-selig/ads/coord_database.html#F, (Accessed: May 27, 2016).
[20] D. C. Sale, "HARP_Opt User's Guide," National Renewable Energy Laboratory, 2011, [Online]. Available: https://nwtc.nrel.gov/HARP_Opt, (Accessed January 4, 2016).
[21] F. R. Driscoll, G. M. Alsenas, P. P. Beaujean, S. Ravenna, J. Raveling, E. Busold, and C. Slezycki, "A 20 kW open ocean current test turbine," in *Proc. 2008 MTS/IEEE Oceans Conference, Quebec City, Canada, September 15–18, No. OCEANS.2008.5152104*, 2008.
[22] J. VanZwieten, F.R. Driscoll, A. Leonessa, and G. Deane, "Design of a prototype ocean current turbine - Part I: mathematical modeling and dynamics simulation," *Ocean Engineering*, 33 (11-12), 1485-1521, 2006.
[23] N. O. Jensen, "A note on wind generation interaction," Riso National Laboratory, Denmark, 1983.
[24] J. F. Ainslie, "Calculating the flowfield in the wake of wind turbines," *Journal of Wind Engineering and Industrial Aerodynamics*, 27 (1988) 213-224, 1988.
[25] P. Pyakurel, W. Tian, J. H. VanZwieten, and M. Dhanak, "Characterization of the mean flow field in the far wake region behind ocean current turbines", *Journal of Ocean Engineering and Marine Energy*, vol. 3, Issue 2, pp. 113-123, May 2017.
[26] I. Masters, A. J. Williams, M. Edmunds, P. Pyakurel, and J. H. VanZwieten, "The effects of turbulence intensity on the downstream performance of horizontal axis tidal stream turbines," in *VII International Conference on Computational Methods in Marine Engineering*, MARINE 2017.
[27] V. S. Neary, B. Gunawan, C. Hill and L. P. Chamorro, "Near and far field flow disturbances induced by model hydrokinetic turbine: ADV and ADP comparison," *Renewable Energy*, no. 60, pp. 1-6, 2013.
[28] T. Stallard, R. Collings, T. Feng, and J. Whelan, "Interactions between tidal turbine wakes: experimental study of a group of three-bladed rotors," *Phil Trans R Soc A*, 371: 20120159, 2013. [Online]. Available: http://rsta.royalsocietypublishing.org/content/roypta/371/1985/20120159.full.pdf (Accessed: Apr. 27, 2017)
[29] P. Mycek, B. Gaurier, G. Germain, G. Pinon, and E. Rivoalen, "Experimental study of the turbulence intensity effects on marine current turbines behaviour, Part I: Two interacting turbines," *Renewable Energy*, 66 (2014) 729-746, 2014.
[30] K. E. Johnson, "Adaptive Torque Control of Variable Speed Wind Turbines," National Renewable Energy Laboratory, 2004.
[31] T. Ngo, C. Sultan, J. H. Van Zwieten, N. I. Xiros, "Variance Constrained Cyclic Blade Control of Moored Ocean Current Turbines," in *Proc American Control Conference*, Boston, MA, USA, July 4-6, 2016.
[32] J. Thomson, B. Polagye, V. Durgesh, M. C. Richmond, "Measurements of Turbulence at Two Tidal Energy Sites in Puget Sound, WA," *IEEE Journal of Oceanic Engineering*, vol. 37, No. 3, July 2012.